Microscopic model realization of d-wave pseudospin current order in Sr$_2$IrO$_4$

Jin-Wei Dong,[1,2,3] Yun-Peng Huang,[4] Ziqiang Wang,[5,*] and Sen Zhou[1,2,6,†]

[1]*CAS Key Laboratory of Theoretical Physics, Institute of Theoretical Physics, Chinese Academy of Sciences, Beijing 100190, China*
[2]*School of Physical Sciences, University of Chinese Academy of Sciences, Beijing 100049, China*
[3]*Anhui Province Key Laboratory of Condensed Matter Physics at Extreme Conditions,*
High Magnetic Field Laboratory, Chinese Academy of Sciences, Hefei 230031, China
[4]*Beijing National Laboratory for Condensed Matter Physics and Institute of Physics, Chinese Academy of Sciences, Beijing 100190, China*
[5]*Department of Physics, Boston College, Chestnut Hill, MA 02467, USA*
[6]*CAS Center for Excellence in Topological Quantum Computation,*
University of Chinese Academy of Sciences, Beijing 100049, China

The d-wave pseudospin current order (dPSCO) with staggered circulating pseudospin current has been proposed as the hidden electronic order to describe the unexpected breaking of spatial symmetries in stoichiometric Sr$_2$IrO$_4$ and the unconventional pseudogap phenomena in electron doped Sr$_2$IrO$_4$. However, a microscopic model for the emergence of dPSCO is still lacking. The nearest neighbor Coulomb repulsion V, which is expected to be significant in Sr$_2$IrO$_4$ due to the large spatial extension of the Ir $5d$ orbitals, is capable of driving dPSCO on the mean-field level, albeit the latter is energetically degenerate to the staggered flux phase with circulating charge current. We find the in-plane anisotropy Γ_2 in the effective superexchange interaction between $J_{\text{eff}} = \frac{1}{2}$ pseudospins, originating from the cooperative interplay between Hund's rule coupling and spin-orbit coupling of Ir $5d$ electrons, is able to lift the degeneracy and stabilize the pseudospin currents. The effective single-orbital model of $J_{\text{eff}} = \frac{1}{2}$ electrons, including onsite Coulomb repulsion U, nearest neighbor Coulomb repulsion V, and the in-plane anisotropy Γ_2, is then studied. We obtain the mean-field ground states, analyze their properties, and determine the phase diagram of stoichiometric Sr$_2$IrO$_4$ in the plane spanned by U and V at a fixed Γ_2. We demonstrate the realization of dPSCO, as well as its competition and coexistence with antiferromagnetism. Remarkably, we find the coexistence of dPSCO and antiferromagnetism naturally leads to spin bond nematicity, with the spin directions of these three orders forming nontrivial chirality. Furthermore, we show that the emergence of the coexistent state and its chirality can be tuned by carrier doping.

I. INTRODUCTION

The layered square-lattice iridate Sr$_2$IrO$_4$ has recently attracted much attention partly due to its close resemblance to the high-temperature cuprate superconductors [1–12]. It is isostructural to La$_2$CuO$_4$ and the stoichiometric Sr$_2$IrO$_4$ becomes a canted antiferromagnetic (AFM) insulator below the Néel temperature $T_N \simeq 230$ K [1, 2]. The magnetic excitations are well described by pseudospin-$\frac{1}{2}$ Heisenberg model on the square lattice, with strong AFM exchange coupling $J \simeq 60$ meV [13, 14]. This is believed to be the essential physics of the cuprates and thus naturally leads to the expectation that Sr$_2$IrO$_4$ can be another platform for unconventional high-temperature superconductivity upon carrier doping [15–18]. Although there is not yet firm evidence for superconductivity, a remarkable range of cuprate phenomenology has been observed in electron- and hole-doped Sr$_2$IrO$_4$, including Fermi surface pockets [19], Fermi arcs [20], pseudogaps [21–23], and V-shaped tunneling spectra that potentially signals d-wave superconductivity [24, 25].

At stoichiometry, neutron and resonant X-ray measurements reveal that the magnetic moments in the canted AFM insulator are aligned in the basal ab plane, with their directions tracking the staggered IrO$_6$ octahedra rotation about the c axis due to strong spin-orbit coupling [26–30]. The resulting net ferromagnetic moment of each layer is shown to order in a + − −+ pattern along the c axis [2, 31]. This magnetic ground state belongs to a centrosymmetric orthorhombic magnetic point group $2/m1'$ with spatial C_{2z} rotation, inversion,

and time-reversal symmetries (TRS) [32, 33]. Recent optical second-harmonic generation experiments [32, 34], however, reported evidence of unexpected breaking of spatial rotation and inversion symmetries, pointing to the existence of a symmetry-breaking hidden order. It is further supported by polarized neutron diffraction [35] and muon spin relaxation measurements [36] which revealed the breaking of TRS. Intriguingly, magnetic resonant X-ray scattering measurements conducted on the electron-doped Sr$_2$IrO$_4$ have uncovered a unidirectional spin density wave in the pseudogap phase [37], further supporting the idea that the pseudogap is associated with a symmetry-breaking hidden order. It was argued that the broken symmetries can be caused by loop currents [32, 35, 36, 38] which were proposed to account for the pseudogap physics in cuprates [39–41]. However, the oxygen $2p$ states in Sr$_2$IrO$_4$ are much further away from the Fermi level than those in the cuprates [1, 42], making it disadvantageous to develop the loop currents that requires low-energy oxygen $2p$ states.

The d-wave pseudospin current order (dPSCO), with pseudospin-up electrons staggered circulating along one direction and pseudospin-down electrons in the opposite direction, has been proposed as an alternative candidate for the hidden electronic order in Sr$_2$IrO$_4$ [43]. Symmetry analysis shows that the coexistence of dPSCO and canted AFM with a particular c-axis stacking pattern has the symmetries consistent with all available experimental observations on the stoichiometric Sr$_2$IrO$_4$ below the Néel temperature [44]. This coexistent phase is a magnetoelectric state that breaks twofold

rotation, spatial inversion, and TRS [44]. In addition, it can account for the observed splitting of bands [19] at $(\pi, 0)$ whose twofold degeneracy is otherwise protected by certain lattice symmetries [43, 45, 46]. Upon sufficient electron doping such that the magnetism is completely suppressed, dPSCO produces Fermi pockets and Fermi arcs in the nonmagnetic electron-doped Sr_2IrO_4 [43], in good agreement with the pseudogap phenomena revealed by angle-resolved photoemission and scanning tunneling microscopy measurements [19–21, 24]. While describing remarkably well the unexpected symmetry properties and the unconventional quasiparticle behaviours observed in both stoichiometric and electron-doped Sr_2IrO_4, the physical origin of dPSCO is unclear and a microscopic model for its emergence is still lacking.

In this work, we discuss the emergence of dPSCO in an effective single-orbital model for pseudospin-$\frac{1}{2}$ electrons of Sr_2IrO_4 in the local basis (see Fig. 1a) tracking the staggered IrO_6 octahedra rotation, in which the canted AFM becomes a perfect Néel order [15, 47]. Hereinafter, we replace dPSCO by dSCO (d-wave spin current order) for convenience. Due to the large spatial extension of the Ir $5d$ orbitals, the off-site Coulomb repulsions are significant in Sr_2IrO_4 and expected to play important role in the development of dSCO. Indeed, it has been shown on half-filled honeycomb lattice that off-site Coulomb repulsions can produce dSCO with staggered spin current on the mean-field level [48]. It has the continuous global SO(3) symmetry associated with the rotation of the spin direction, and energetically degenerate with the staggered flux phase (SFP) with circulating charge current, leading to spin Hall effect and anomalous Hall effect, respectively. TRS is broken in SFP but preserved in dSCO, and thus these two states can never coexist. It is argued that quantum fluctuations lifts the degeneracy and favors spin current over charge current [48].

Interestingly, we note that the in-plane anisotropy Γ_2 in the effective superexchange interactions between the $J_{\text{eff}} = \frac{1}{2}$ pseudospins, originating from the cooperative interplay between Hund's rule coupling and spin-orbit coupling of the Ir $5d$ electrons [47], can lift the degeneracy between SFP and dSCO within mean-field theories. Furthermore, it breaks the SO(3) rotation symmetry of dSCO down to C_{4z} by orientating the spins of dSCO along one of the four easy axes, i.e., $[\pm 1, \pm 1, 0]$. This motivates us to investigate the realization of dSCO in a concrete effective single-orbital t-U-V-Γ_2 model of pseudospin-$\frac{1}{2}$ electrons for Sr_2IrO_4, where t denotes the kinetic hoppings, U for on-site Coulomb repulsion, V for nearest-neighbor (nn) Coulomb repulsion, and Γ_2 for the in-plane anisotropy of pseudospins.

We discuss the emergence of dSCO in the t-U-V-Γ_2 model, and investigate its competition and coexistence with AFM. The rest of the paper is organized as follows. Sec. II introduces the effective single-orbital t-U-V-Γ_2 model for pseudospin-$\frac{1}{2}$ electrons in Sr_2IrO_4. The onsite Coulomb repulsion U is treated by SU(2) spin-rotation invariant slave-boson mean-field theory, while interactions on nn bonds, V and Γ_2, are mean-field decoupled into bond channels. In
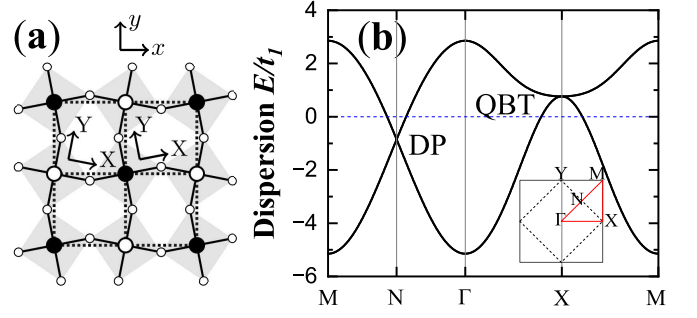

FIG. 1. (a) Schematic picture of one IrO_2 layer. Large filled or open circles denote the Ir atoms on the two sublattices, and small open circles are oxygens. Lowercase x, y and capital X, Y indicate, respectively, the global and sublattice-dependent local cubic axis. (b) Tight-binding band structure of the free electrons, displaying a DP at N and a QBT at X point. The inset in (b) shows the one-Ir BZ (solid black lines), the reduced BZ (dotted black lines), and the high-symmetry points labeled by $\Gamma = (0, 0)$, $X = (\pi, 0)$, $Y = (0, \pi)$, $M = (\pi, \pi)$, and $N = (\pi/2, \pi/2)$.

Sec. III, the t-U-V-Γ_2 model is solved self-consistently at half-filling for stoichiometric Sr_2IrO_4. We obtain the mean field ground states, analyze their properties, and determine the phase diagram at a fixed nonzero Γ_2. The phase diagram consists of paramagnetic (PM), AFM, dSCO, and the coexistent state involving the latter two. We note that the coexistent state breaks the C_{4z} rotation symmetry of $J_{\text{eff}} = \frac{1}{2}$ pseudospins, and naturally leads to spin bond nematicity (sBN) with nontrivial chirality. We then study the doping evolution of these states and illustrate that the emergence of coexistent state and its chirality can be tuned by the carrier doping. Possible connections to experimental observations are also discussed. Summaries are presented in Sec. IV.

II. MODEL AND METHOD

The t-U-V-Γ_2 model. We start with an effective square lattice single-orbital t-U-V-Γ_2 model for the pseudospin-$\frac{1}{2}$ electrons in the local basis depicted in Fig. 1a that tracks the staggered IrO_6 octahedra rotation in Sr_2IrO_4,

$$\hat{H} = -\sum_{ij,\alpha} t_{ij} c_{i\alpha}^\dagger c_{j\alpha} + U \sum_i \hat{n}_{i\uparrow} \hat{n}_{i\downarrow} \quad (1)$$
$$+ V \sum_{\langle ij \rangle} \hat{n}_i \hat{n}_j + \Gamma_2 \sum_{\langle ij \rangle} \tau_{ij} (\hat{S}_i^x \hat{S}_j^x - \hat{S}_i^y \hat{S}_j^y),$$

where $\tau_{ij} = (-1)^{i_y + j_y}$ is the standard d-wave form factor on nn bonds, $c_{i\alpha}^\dagger$ creates a pseudospin-α ($\alpha = \uparrow, \downarrow$) electron at site i, the density operators $\hat{n}_{i\alpha} = c_{i\alpha}^\dagger c_{i\alpha}$, $\hat{n}_i = \sum_\alpha \hat{n}_{i\alpha}$, and the pseudospin operator $\hat{S}_i^\eta = \frac{1}{2} \sum_{\alpha\beta} c_{i\alpha}^\dagger \sigma_{\alpha\beta}^\eta c_{i\beta}$ with σ^η the Pauli matrices for $\eta = x, y, z$. To describe the low-energy quasiparticle dispersion (Appendix A), the hopping parameters are chosen according to $t_{ij} = (t_1, t_2, t_3) = (218, 52, -18)$ meV for the first, second, and third nn hopping, respectively. Fig. 1b

shows the tight-binding dispersion along the high-symmetry path in the reduced Brillouin zone (BZ), displaying the characteristic Dirac point (DP) at N and quadratic band touching (QBT) at X point. For this set of band parameters, the QBT is higher in energy than DP by $4t_2 - 8t_3 = 352$ meV. In Eq. (1), U and V are the onsite and nn Coulomb repulsions, and Γ_2 is the in-plane anisotropy for $J_{\text{eff}} = \frac{1}{2}$ pseudospins. It has been shown that Γ_2 is generated by the cooperative interplay between Hund's rule coupling and spin-orbit coupling of Ir $5d$ electrons, and induces a small in-plane magnetic gap via quantum fluctuations [47].

Mean-field theories. To treat the onsite interaction non-perturbatively and consider in-plane magnetic order conveniently, we use the Kotliar-Ruckenstein slave-boson formulation with SU(2) spin-rotation invariance [49–52], in which the physical electron operator is written as

$$c_\alpha = Z_{\alpha\beta}f_\beta, \quad \mathbf{Z} = \mathbf{L}^{-1/2}\left(e^\dagger\mathbf{p} + \bar{\mathbf{p}}^\dagger d\right)\mathbf{R}^{-1/2}, \tag{2}$$

where f_α is a spin-$\frac{1}{2}$ fermion operator, and e, d, and $\mathbf{p}$ are boson operators describe the holon, doublon, and singly occupied sites. The SU(2) spin-rotation invariance is achieved by the 2×2 matrix representation of the singly occupied site, $\mathbf{p}$, with element $p_{\alpha\beta} = \frac{1}{\sqrt{2}}\sum_{\mu=0,x,y,z}p_\mu\sigma^\mu_{\alpha\beta}$, and its time-reversal transformation $\bar{\mathbf{p}} = \hat{T}\mathbf{p}\hat{T}^{-1}$. The 2×2 matrix operator $\mathbf{L} = (1 - d^\dagger d)\sigma^0 - \mathbf{p}^\dagger\mathbf{p}$, $\mathbf{R} = (1 - e^\dagger e)\sigma^0 - \bar{\mathbf{p}}^\dagger\bar{\mathbf{p}}$, with σ^0 the 2×2 identity matrix. This form ensures the spin rotation invariance and the correct noninteracting limit within the mean-field approximation [51]. The intersite interactions on nn bonds, V and Γ_2, are rewritten in terms of Hubbard-Stratonivich fields $\hat{\chi}^\mu_{\langle ij\rangle} = \sum_{\alpha\beta}f^\dagger_{i\alpha}\sigma^\mu_{\alpha\beta}f_{j\beta}$, $\mu = 0, x, y, z$ [48]. The charge density fields corresponding to the direct Hartree decoupling of V are neglected to avoid double-counting, since their contribution is already included in the LDA [53]. Furthermore, it is easy to show that the spin density fields for the in-plane anisotropy Γ_2 are irrelevant in the two-sublattice states considered in this work. As a result, the Hamiltonian becomes

$$\widetilde{H} = -\sum_{ij,\alpha\beta\gamma}t_{ij}f^\dagger_{i\alpha}Z^\dagger_{i,\alpha\gamma}Z_{j,\gamma\beta}f_{j\beta} + U\sum_i d^\dagger_i d_i + \sum_i \lambda_i \hat{Q}_i \tag{3}$$

$$+ \sum_{i,\mu}\lambda^\mu_i\hat{Q}^\mu_i - \sum_{\langle ij\rangle}\left\{\frac{V}{2}\sum_\mu|\hat{\chi}^\mu_{ij}|^2 + \frac{\Gamma_2}{4}\tau_{ij}\left[|\hat{\chi}^x_{ij}|^2 - |\hat{\chi}^y_{ij}|^2\right]\right\},$$

where λ_i and λ^μ_i ($\mu = 0, x, y, z$) are Lagrange multipliers introduced to enforce the local constraints for the completeness of the Hilbert space

$$\hat{Q}_i = e^\dagger_i e_i + d^\dagger_i d_i + \text{tr}(\mathbf{p}^\dagger_i\mathbf{p}_i) - 1 = 0, \tag{4}$$

and the equivalence between the fermion and boson representations of the particle and spin densities

$$\hat{Q}^\mu_i = \text{tr}(\sigma^\eta\mathbf{p}^\dagger_i\mathbf{p}_i) + 2\delta_{\mu,0}d^\dagger_i d_i - \sum_{\alpha\beta}f^\dagger_{i\alpha}\sigma^\mu_{\alpha\beta}f_{i\beta} = 0. \tag{5}$$

The saddle-point solution of the functional-integral for Eq. (3) corresponds to condensing all boson fields $\{e_i, d_i, p_{i\mu}, \lambda_i, \lambda^\mu_i,$ $\chi^\mu_{\langle ij\rangle}\}$ and determining their values self-consistently by minimizing the state energy $\langle\widetilde{H}\rangle$.

The onsite and nn Coulomb repulsions, U and V, would produce, respectively, magnetic and bond orders at sufficient strengths. We consider two-sublattice solutions where onsite boson fields condense uniformly on each sublattice $\nu = A$ or B. Explicitly, on site $i \in \nu$, $e_i = e_\nu$, $d_i = d_\nu$, $p_{i\mu} = p_{\nu\mu}$, $\lambda_i = \lambda_\nu$, and $\lambda^\mu_i = \lambda^\mu_\nu$. Consequently, the local magnetic moment $\mathbf{m}_i = \mathbf{m}_\nu = (m^x_\nu, m^y_\nu, m^z_\nu)$, with component $m^\eta_\nu = \text{tr}(\sigma^\eta\mathbf{p}^\dagger_\nu\mathbf{p}_\nu)$, where a g-factor of 2 has been used. Self-consistent calculations converge to charge uniform states with, if magnetism developed, perfect Néel order in the local basis tracking the IrO$_6$ staggered rotation. As a result, $e_\nu = e$, $d_\nu = d$, $\lambda_\nu = \lambda$, $p_{\nu0} = p_0$, $\lambda^0_\nu = \lambda^0$, and $p_{A\eta} = -p_{B\eta} = p_\eta$, $\lambda^\eta_A = -\lambda^\eta_B = \lambda^\eta$ for $\eta = x, y, z$. Consequently, the magnetic moment $\mathbf{m}_A = -\mathbf{m}_B = \mathbf{m}$. Similarly, the condensation of boson fields on nn bonds can be expressed as a combination of s- and d-wave components

$$\chi^\mu_{\langle ij\rangle} = \left(\chi'_{\mu,s} + i\chi''_{\mu,s}\right) + \tau_{ij}\left(\chi'_{\mu,d} + i\chi''_{\mu,d}\right), \quad i \in A \text{ and } j \in B, \tag{6}$$

where $\chi'_{\mu,s}$ ($\chi''_{\mu,s}$) and $\chi'_{\mu,d}$ ($\chi''_{\mu,d}$) are the real and imaginary parts of the $s(d)$-wave component. In the charge-uniform two-sublattice solutions, the contributions to the state energy per site from V and Γ_2 are given by, respectively,

$$E_V = -V\sum_\mu\left(\chi'^2_{\mu,s} + \chi''^2_{\mu,s} + \chi'^2_{\mu,d} + \chi''^2_{\mu,d}\right), \tag{7}$$

$$E_{\Gamma_2} = \Gamma_2\left(\chi'_{y,s}\chi'_{y,d} + \chi''_{y,s}\chi''_{y,d} - \chi'_{x,s}\chi'_{x,d} - \chi''_{x,s}\chi''_{x,d}\right). \tag{8}$$

Clearly, in-plane anisotropy Γ_2 tends to bring mixture of s- and d-wave components in the $\mu = x, y$ bond orders to gain energy and, as a result, breaks the SO(3) rotational symmetry of spin currents down to C_{4z} with four easy axes along $[\pm 1, \pm 1, 0]$. We note that nonzero $\chi''_{0,s}$ brings charge currents flowing into or out of a lattice site from all the four connecting bonds, which violate the charge conservation and thus physically prohibited. In contrast, nonzero $\boldsymbol{\chi}_{s\text{SCO}} = (\chi''_{x,s}, \chi''_{y,s}, \chi''_{z,s})$ $\equiv \chi_{s\text{SCO}}\hat{e}_{s\text{SCO}}$ that violates the spin conservation on each lattice site by generating s-wave spin current is however allowed at finite in-plane anisotropy Γ_2 since the presence of the latter requires the existence of spin-orbit coupling [47]. Similarly, the real parts of d-wave bond orders introduce charge bond nematicity (cBN) $\chi_{c\text{BN}} = \chi'_{0,d}$ [53] and sBN $\boldsymbol{\chi}_{s\text{BN}} = (\chi'_{x,d}, \chi'_{y,d}, \chi'_{z,d}) \equiv \chi_{s\text{BN}}\hat{e}_{s\text{BN}}$, while the imaginary parts of d-wave bond orders generate SFP $\chi_{\text{SFP}} = \chi''_{0,d}$ and dSCO with $\boldsymbol{\chi}_{d\text{SCO}} = (\chi''_{x,d}, \chi''_{y,d}, \chi''_{z,d}) \equiv \chi_{d\text{SCO}}\hat{e}_{d\text{SCO}}$ for spins along $\hat{e}_{d\text{SCO}}$ direction.

To this end, in order to obtain all the possible states, we use different initial conditions for solving the self-consistency equations numerically. Besides PM, AFM, and dSCO, we also encounter converged metallic solutions of coexisting AFM and dSCO, which induces additional sBN and brings about interesting chirality for the spin directions of these three orders. When more than one converged states exist at a given set of parameters, we compare their energies to determine the true ground state.
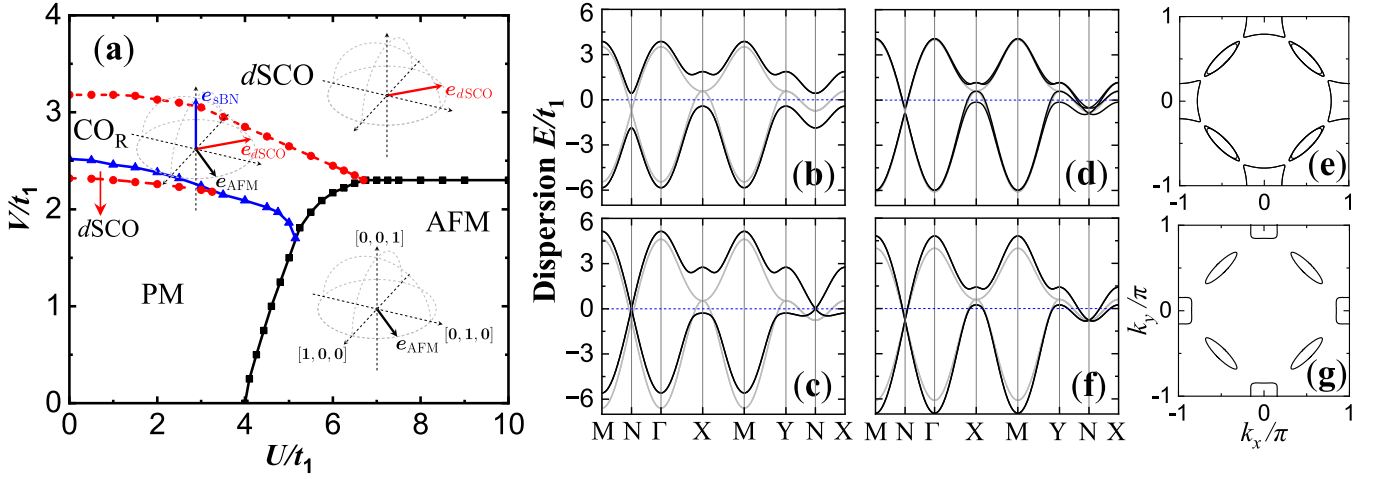
FIG. 2. (a) Ground state phase diagram of half-filled t-U-V-Γ_2 model with fixed $\Gamma_2 = 0.2t_1$. Solid and dashed lines denote, respectively, phase boundaries of first-order and continuous transitions. Insets display the spin directions of order parameters, i.e., $\hat{e}_{AFM}$, $\hat{e}_{dSCO}$, and $\hat{e}_{sBN}$, in each ground states. Electronic structures of the nonparamagnetic ground states (black lines) along high-symmetry path at Coulomb interactions $(U, V) = (6, 1.6)t_1$ for the insulating AFM (b), $(6, 3)t_1$ for the semimetallic dSCO (c), $(5, 2)t_1$ for metallic CO$_R$ (d), and $(1, 2.4)t_1$ for the metallic dSCO (f). Grey lines denote the band dispersion of the PM states converged at the same parameters. The corresponding Fermi surfaces of (d) and (f) are shown in, respectively, (e) and (g).

III. RESULTS AND DISCUSSIONS

Phase diagram at half filling. We first explore the zero-temperature phase structure and the formation of dSCO in the half-filled t-U-V-Γ_2 model for a given in-plane anisotropy. At $\Gamma_2 = 0.2t_1$, the ground state phase diagram is presented in Fig. 2a in the plane spanned by the on-site Coulomb repulsion U and nn Coulomb repulsion V. It consists of PM, AFM, dSCO, and CO$_R$. Here, CO$_R$ refers to the coexisting state of AFM, dSCO, and sBN, with the subscript denotes the right-handed chirality formed by the spin directions of these three orders. The solid and dashed lines denote, respectively, a first-order and a continuous phase transition between two neighboring phases, and the boundaries are determined by comparing the state energies of different phases.

PM and AFM. In the regime near the phase diagram origin where neither U nor V is strong enough to produce magnetic or bond orders, the ground state is a PM metal with the bandwidth renormalized by electron correlations. Increasing U at small V, the PM metal gives way to the AFM insulator at a critical U via a first-order transition. As shown in Fig. 2a, the critical U increases as one enhances the nn Coulomb repulsion V, since the latter effectively enlarges the bandwidth. The AFM gaps out the DP and QBT simultaneously, resulting to a band dispersion displayed in Fig. 2b at $(U, V) = (6, 1.6)t_1$. Since Γ_2 does not generate any in-plane magnetic anisotropy on the mean-field level [47] and all other terms in the t-U-V-Γ_2 model are invariant under spin rotation, the moment direction of AFM obtained here thus has the SO(3) rotation symmetry. Inclusion of out-of-plane anisotropy Γ_1, which is shown to be present in Sr$_2$IrO$_4$ [47], would break SO(3) symmetry down to SO(2) with easy xy-plane. Furthermore, when

coexisting with dSCO, as we shall show later, the spin rotation symmetry is further reduced to C_{4z} with four equivalent easy-axes along $[\pm 1, \pm 1, 0]$, consistent with experimental observations and theoretical results in more sophisticated five-orbital models [26–28, 54–59]. In this work, we neglect Γ_1 in the Hamiltonian for simplicity and, without loss of generality, fix the moment direction along $[1, 1, 0]$, unless otherwise noted.

Interestingly, we note that AFM could not be stabilized by any U when nn Coulomb repulsion is large, i.e., $V \gtrsim 2.3t_1$, as shown in the phase diagram Fig. 2a. In the strongly coupling theory, the dynamically generated AFM Zeeman field scales with the average kinetic energy instead of U [60]. This effectively sets a upper limit on the energy gain via the formation of AFM. On the other hand, the energy gain of bond order, if developed, is on the order of V, as shown clearly in Eq. (7). Therefor, AFM is unable to compete with bond orders, dSCO in particular here, when V is sufficiently large, regardless of how strong on-site U is.

dSCO. When V is large, it drives charge or spin currents on the nn bonds and consequently leads to SFP or dSCO separately. These two states are energetically degenerate and share the identical band structure in the absence of Γ_2, and dSCO has SO(3) rotation symmetry associated with the spin direction of the spin current. The SFP breaks TRS while dSCO does not, and thus these two states can never coexist with each other. We note that the in-plane anisotropy Γ_2 is able to lift the degeneracy within the mean-field theory and stabilize dSCO with circulating spin currents as the ground state. Furthermore, in the presence of Γ_2, the SO(3) rotation symmetry of dSCO is broken down to C_{4z} with four equivalent preferred directions along $[\pm 1, \pm 1, 0]$, i.e., $\boldsymbol{\chi}_{dSCO} = (\pm 1, \pm 1, 0)\chi_d''$. The lifting of degeneracy and the lowering of rotation symmetry
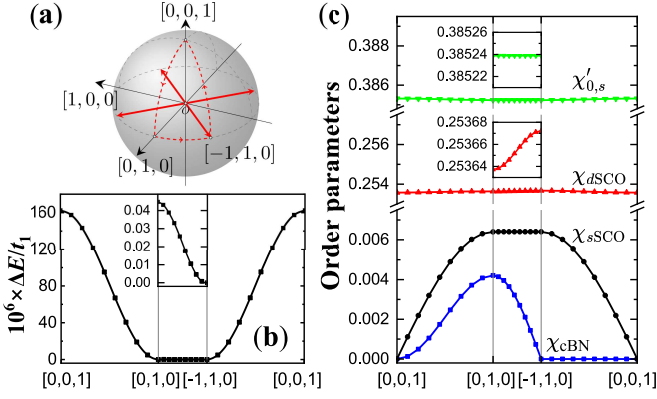
FIG. 3. (a) Path of $\hat{e}_{d\mathrm{SCO}}$ for the variational calculations. (b) The state energy and (c) the magnitudes of various bond orders in dSCO as a function of the pinned spin direction $\hat{e}_{d\mathrm{SCO}}$ displayed in (a). The Coulomb interactions $(U, V) = (6, 3)t_1$.
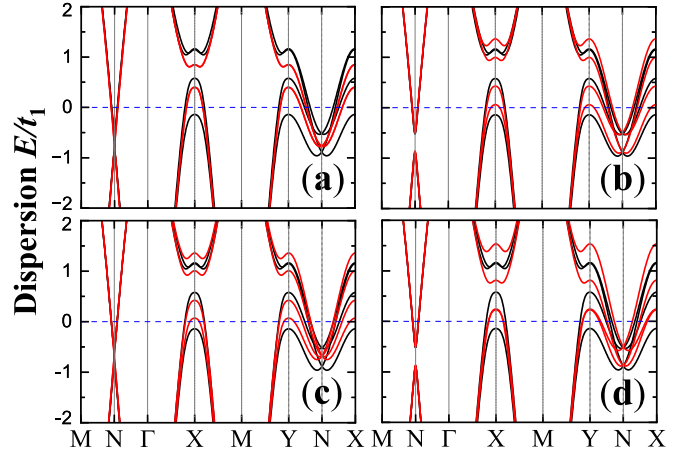

FIG. 4. Low-energy band dispersions (red lines) of (a) the self-consistently converged pure dSCO, (b) CO_R with sBN order manually switched off, (c) CO_R with AFM order manually switched off, and (d) CO_R with the spin direction of sBN manually reversed. Band dispersions of the self-consistently converged CO_R are plotted in black lines for comparison. The Coulomb interactions $(U, V) = (5, 2)t_1$.

are achieved via the development of a s-wave spin current order (sSCO) with the spin direction along $[\pm 1, \mp 1, 0]$ direction, i.e., $\boldsymbol{\chi}_{s\mathrm{SCO}} = (\pm 1, \mp 1, 0)\chi_s''$, which coexists with d-wave $\boldsymbol{\chi}_{d\mathrm{SCO}}$ and lowers the state energy per site in Eq. (8) by $-2\Gamma_2 \chi_s'' \chi_d''$. Due to its d-wave nature, dSCO gaps out the QBT at X but leaves the DP at N unaltered. At sufficient strong V where the dSCO gap is large, it gives rise to a Dirac semimetal with vanishing density of states at Fermi level, as illustrated in the band dispersion at $(U, V) = (6, 3)t_1$ shown in Fig. 2c.

In order to elaborate on the anisotropy in the spin direction of dSCO in the presence of Γ_2, we have performed variational calculation where an external field is applied to pin the spin direction of spin currents along the desired direction, whereas the elastic part of the external field is excluded in the state energy. As a function of $\hat{e}_{d\mathrm{SCO}}$ pinned along the path shown in Fig. 3a, the state energy per site is plotted in Fig. 3b at $(U, V) = (6, 3)t_1$, with the inset focus on the in-plane anisotropy. For clarity, all energies are shown with respect to $E_{[-1,1,0]}$, i.e., energy of dSCO with $\hat{e}_{d\mathrm{SCO}}$ along $[-1, 1, 0]$. Clearly, $[-1, 1, 0]$ is the most preferred spin direction for dSCO, with a tiny in-plane anisotropy $E_{[0,1,0]} - E_{[-1,1,0]} \simeq 4.5 \times 10^{-8} t_1$ and a relatively large out-of-plane anisotropy $E_{[0,0,1]} - E_{[-1,1,0]} \simeq 1.6 \times 10^{-4} t_1$. The evolution of the amplitudes of various bond orders are displayed in Fig. 3c. It is clear that the in-plane dSCO gain energy via the formation of $\boldsymbol{\chi}_{s\mathrm{SCO}}$, while the $[-1, 1, 0]$ dSCO lowers energy further by the small increasing in its amplitude $\chi_{d\mathrm{SCO}}$.

CO_R. Reducing the nn V from the dSCO phase at small to moderate U, the phase diagram in Fig. 2a shows a wide regime where the ground state possesses simultaneously AFM, dSCO, and sBN orderings. Interestingly, the spin directions of these three orders, $\hat{e}_{\mathrm{AFM}}$, $\hat{e}_{d\mathrm{SCO}}$, and $\hat{e}_{\mathrm{sBN}}$, are perpendicular to each other and form a right-handed chirality, i.e., $(\hat{e}_{\mathrm{AFM}} \times \hat{e}_{d\mathrm{SCO}}) \cdot \hat{e}_{\mathrm{sBN}} = 1$, as displayed in the inset in Fig. 2a. Therefore, we refer to this coexistent state as CO_R hereafter. At $(U, V) = (5, 2)t_1$, the converged CO_R has AFM moment

$m = 0.135\mu_B$, dSCO $\chi_{d\mathrm{SCO}} = 0.117$, and sBN $\chi_{\mathrm{sBN}} = 0.044$, with the electronic structure shown in Fig. 2d. The primary feature of the coexistence lies at X point where the doubly degenerate bands in AFM and dSCO are now split unevenly, unnoticeably small on the conduction bands above the Fermi level but substantially larger on the valence bands crossing the Fermi level. It gains energy by pushing one of the valence band below Fermi level. The corresponding Fermi surfaces is displayed in Fig. 2e, exhibiting two elliptic electron pockets around N points and a square-shaped hole pocket around X and Y points.

To shed light on the emergence of the coexisting CO_R phase, we plot in Fig. 4a the band structure of the would-be pure dSCO self-consistently converged at the same interactions, $(U, V) = (5, 2)t_1$. Clearly, the dSCO gap is not large enough to realize a Dirac semimetal, as the doubly degenerate valence bands cross the Fermi level around X point. This would leads to a large density of states at Fermi level, which is expected to trigger the emergence of AFM and sBN, and hence the stabilization of the coexistent state. To further understand the coexistence and its chirality, we manually switch off the sBN or AFM in the CO_R and plot the resulting electronic structure in, respectively, Fig. 4b and 4c. Clearly, in both cases, the conduction and valence bands split evenly at X point, failing to push one of the valence band below Fermi level and thus could not compete with CO_R in lowering state energy. Furthermore, symmetry analysis conducted in Appendix B shows that combination of any two of dSCO, AFM, and sBN has the same symmetry properties as the coexisting state of all these three orders. This implies that the combination of any two of these three orders would in principal give rise to the emergence of the third order, which has been ver-
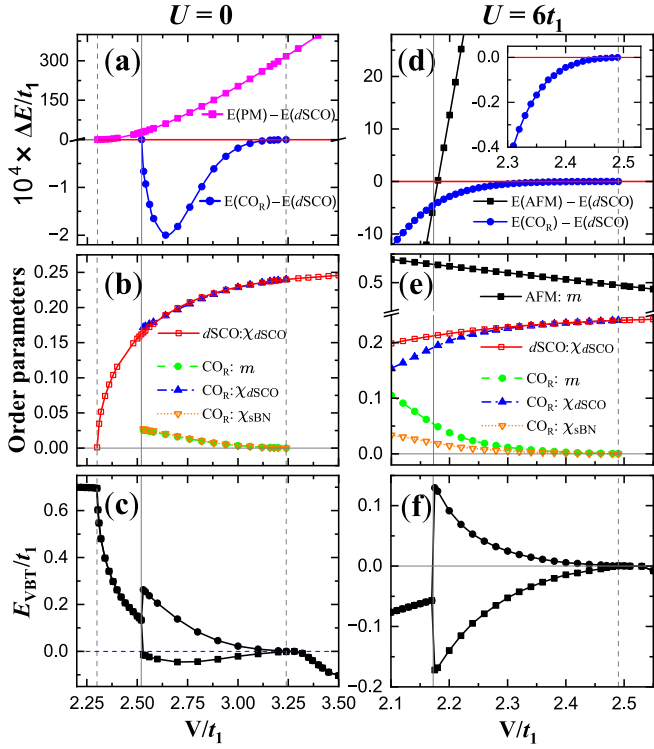
FIG. 5. (a,d) The state energy per site with respect to dSCO, (b,e) the magnitudes of magnetism and bond orders, and (c,f) the locations of valence bond tops at X point, E_{VBT}, as a function of the nn Coulomb repulsion V. The onsite Coulomb repulsion $U = 0$ in left panels and $U = 6t_1$ in right panels.

ified numerically in Appendix B. This is exactly the reason why the regime of CO_R extends to $U = 0$ (this is the case even in the absence of Γ_2) in the phase diagram Fig. 2a, where kinetic magnetism arises in the absence of local repulsion. Next, we manually switch the chirality from right-handed to left-handed, which can be achieved by reversing the spin direction of all three orders or only one of them. The resulting band dispersions are all identical and shown in Fig. 4d. Interestingly, the splitting in the conduction bands is now much larger than that in the valence bands, which is disadvantageous for lowering energy and thus unstable.

We note that, underneath the regime of CO_R in the phase diagram Fig. 2a, there is another small regime for pure dSCO. The band dispersions and corresponding Fermi surfaces are shown in Figs. 2f and 2g at $(U, V) = (1, 2.4)t_1$. The coexistent state could not be stabilized in this regime, as we shall show later, because it fails to push one of the valence band below Fermi level at X point to lower energy.

Phase transitions at half filling. To investigate in detail the phase transitions between different ground states shown in Fig. 2a, we fix onsite Coulomb repulsion $U = 0$ or $6t_1$ and monitor the phase evolution as a function of nn Coulomb repulsion V, focusing on the regions near phase boundaries. The state energies per site with respect to dSCO are compared

in Fig. 5a and 5d. The magnitudes of magnetism and bond orders are shown in Fig. 5b and 5e, and the locations of valence band top E_{VBT}, i.e., the energies of the lower two levels at X point, are plotted in Fig. 5c and 5f.

For $U = 0$, self-consistent calculations at $V \gtrsim 3.24t_1$ can converge to PM and dSCO, with the latter being the ground state with much lower energy, as shown in Fig. 5a. The magnitude of dSCO order is quite large, $\chi_{dSCO} \gtrsim 0.24$ (Fig. 5b), which gaps the QBT by a large gap and consequently leads to a Dirac semimetal shown in Fig. 2c, with the two valence band tops (Fig. 5c) degenerate in energy and lying below the Fermi level. As one reduces nn V, E_{VBT} increase in energy and cross the Fermi level at $V \simeq 3.24t_1$, where the dSCO gives way to CO_R via a second-order transition. AFM and sBN orders start to develop, and their coexistence with dSCO split the two valence bands and push one of them below the Fermi level to lower energy. As shown in Fig. 5c, the evolution of the lower valence band top is nonmonotonic and it is about to cross the Fermi level again at $V \simeq 2.51t_1$. Here the ground state changes from CO_R to dSCO via a first-order transition, as indicated by the kink in state energy (Fig. 5a) and the abrupt disappearance of AFM and sBN orders (Fig. 5b). Reducing V further, the dSCO is suppressed gradually and vanishes at $V \simeq 2.30t_1$ where the ground state becomes PM via a second-order phase transition.

For fixed onsite Coulomb repulsion $U = 6t_1$, the ground state at $V \gtrsim 2.49t_1$ is also a Dirac semimetal, i.e., dSCO with large d-wave gap. Reducing nn V, the ground state first undergoes a second-order transition from dSCO to CO_R at $V \simeq 2.49t_1$ where the doubly degenerate valence band top reaches Fermi level, as shown in Fig. 5f. At $V \simeq 2.17t_1$, AFM sets in via a first-order transition, as shown by the level crossing displayed in Fig. 5d.

Electron-doping evolution of AFM insulator. To make connection to the experimental observations in electron-doped Sr$_2$IrO$_4$ [19–21, 24, 61], it is instructive to study the state evolution with electron doping away from half filling. We fix the in-plane anisotropy $\Gamma_2 = 0.2t_1$ and the Coulomb repulsions $(U, V) = (6, 1.6)t_1$, where the ground state at stoichiometry is the insulating AFM, as shown in Fig. 2a. As a function of electron doping x away from the half filling, the ground state undergoes successively phase transitions from the AFM to dSCO at $x \simeq 0.09$, to a coexistent state with left-handed chirality (CO_L) at $x \simeq 0.23$, and finally to PM at $x \simeq 0.32$, as displayed in Fig. 6a. The energies per site of converged states at different electron doping are summarized in Fig. 6b, with respect to the energy of the PM phase. In addition to the four ground states shown in Fig. 6a, we managed to converge to the cBN state in the electron doping range $0.18 \leq x \leq 0.31$, but it is always higher in energy and fails to present itself as a ground state. The features of level-crossing between these four ground states in Fig. 6b indicate that the three successive phase transitions are all of first-order. Fig. 6c shows the amplitudes of AFM moment and bond orders in the nonparamagnetic phases.

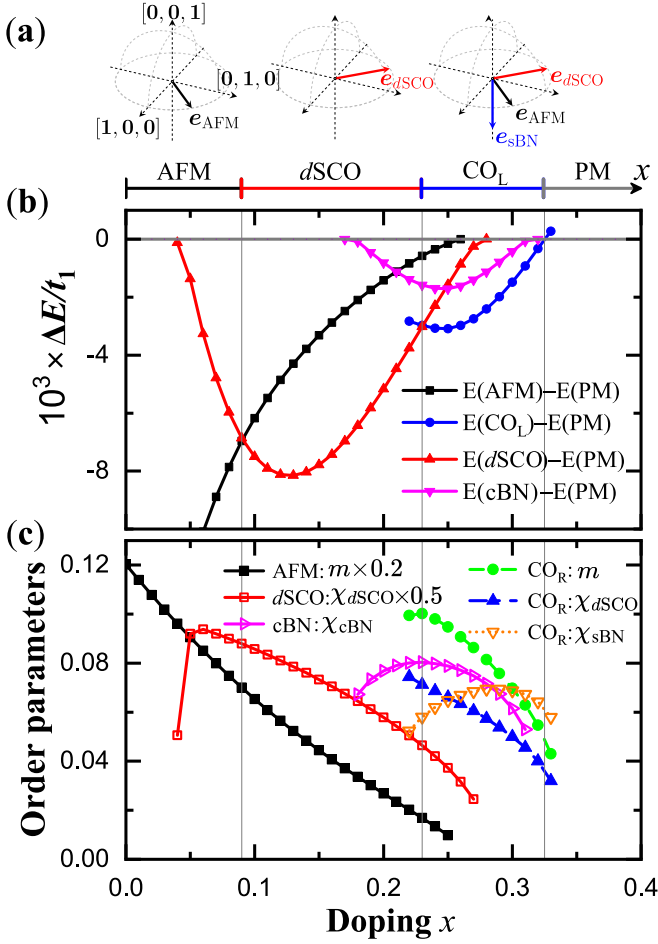The band dispersions and corresponding Fermi surfaces of

(a)

(b)

(c)

FIG. 6. (a) Zero-temperature phase diagram as a function of electron doping, with the insets show the spin directions of AFM, dSCO, and sBN orders. (b) Energy per site of converged states with respect to PM state. (c) Magnitudes of the magnetic and bond orders in nonparamagnetic phases. Here the in-plane anisotropy $\Gamma_2 = 0.2t_1$ and the Coulomb repulsions $(U, V) = (6, 1.6)t_1$.

FIG. 7. Band dispersions (black lines) and corresponding Fermi surfaces of (a) AFM at $x = 0.04$, (b) dSCO at $x = 0.1$, and (c) CO$_L$ at $x = 0.25$. The grey lines in (a) and (c) denote the electronic structure of dSCO converged at the corresponding electron doping.

AFM at $x = 0.04$, dSCO at $x = 0.1$, and CO$_L$ at $x = 0.25$ are plotted in Fig. 7. At half filling $x = 0$, the ground state is an AFM insulator. In the $x = 0.04$ electron-doped AFM, additional electrons go to the bottom of conduction bands around N point and give rise to the elliptic electron pockets showing in Fig. 7a. The dSCO away from half filling in Fig. 7b is a doped Dirac semimetal as the d-wave order gaps only the QBT but leave the Dirac point unaltered. Increasing electron doping x further, the chemical potential moves upwards to accommodate more electrons, and the dSCO order decreases in amplitude as well. As a result, the bottom of the conduction bands near X point get closer to the Fermi level. However, the coexistent state sets in as the ground state before the bottom of the conduction bands reach the Fermi level. The coexistence split the doubly degenerate conduction band bottoms at X point and push one of them below Fermi level to lower energy, as shown in Fig. 7c. Interestingly, this coexistent state
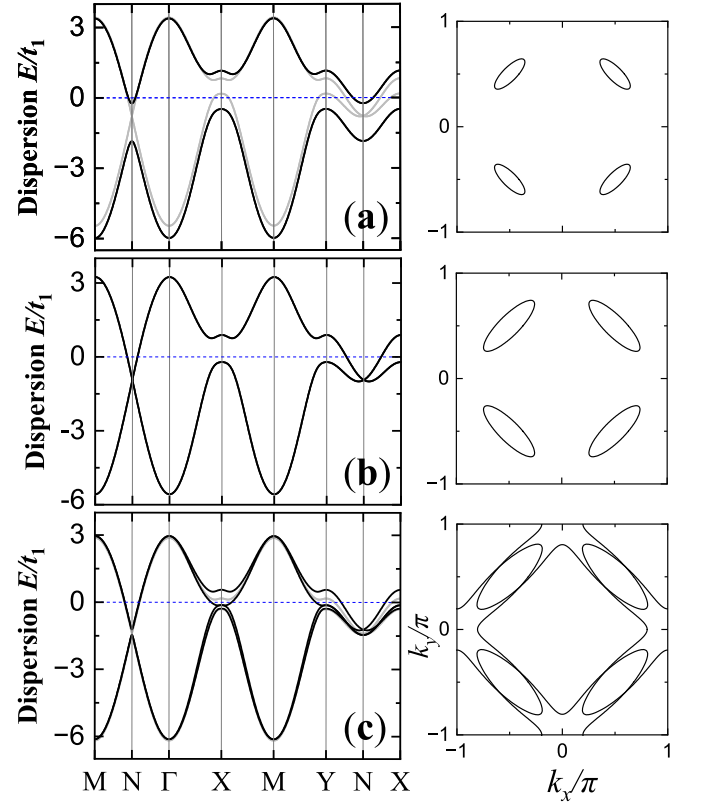
tends to split more the conduction band, thus its chirality is left-handed with $(\hat{e}_{AFM} \times \hat{e}_{dSCO}) \cdot \hat{e}_{sBN} = -1$, instead of right-handed for the coexistent state at half-filling.

Manipulation of chirality by carrier doping. We have shown that when the valence band top or conduction band bottom near X point is above and close to the Fermi level in dSCO phase, coexistent state can be stabilized by splitting the corresponding bands, pushing one of them below Fermi level, and thus lowering the ground state energy. Furthermore, the chirality of the coexistent state manifests itself in the splitting of the bands, CO$_R$ splits mainly the valence bands while CO$_L$ splits more the conduction bands, as shown clearly in Figs. 2d and 7c. It thus suggests that the emergence of coexistent state and its chirality can potentially be manipulated by gate-voltage or carrier doping. To demonstrate it, we start with a Dirac semimetal at half filling by setting $(U, V) = (6, 3)t_1$, where the large dSCO order produces a wide energy gap near X point, as shown in Fig. 2c. The resulting valence band top is below Fermi level and the conduction band bottom is quite far away from the Fermi level, neither of them can trigger the development of coexistent state and the ground state is thus a Dirac semimetal with pure dSCO. Electron- and hole-doping would move the Fermi level, respectively, upwards and down-
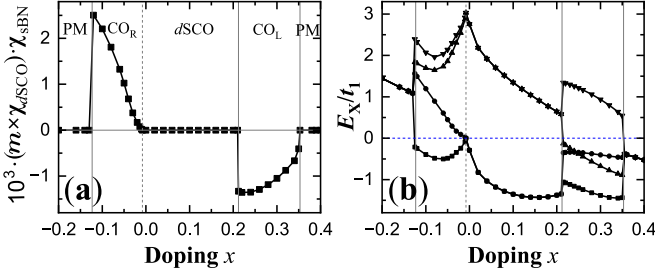
FIG. 8. Doping dependence of (a) the ground state chirality ($m \times \chi_{dSCO}$) · χ_{sBN} and (b) the four energy levels at X point. The Coulomb repulsions $(U, V) = (6, 3)t_1$.

wards, and dSCO is expected to give its way to coexistent state with different chirality at critical doping concentrations.

The state evolution of the Dirac semimetal is summarized in Fig. 8 as a function of carrier doping x, with positive x stands for electron doping and negative x for hole doping. The doping dependence of the ground state chirality ($m \times \chi_{dSCO}$)·χ_{sBN} is displayed in Fig. 8a. It obtains a nonzero value only in the coexistent state, positive in CO_R with right-handed chirality and negative in CO_L with left-handed chirality. Clearly, CO_R and CO_L can be realized separately by hole- and electron-doping a Dirac semimetal. Fig. 8b shows the doping evolution of the four energy levels at X point. As electrons doped into the Dirac semimetal, the Fermi level gets closer to the conduction band bottom, i.e, the upper two levels at X point, and dSCO gives its way to CO_L via a first-order transition at critical doping $x \simeq 0.21$ where the coexistence splits mainly the conduction bands and pushes one of the conduction band bottom below Fermi level. The CO_L becomes unstable with respect to PM at $x \gtrsim 0.35$. On the other hand, hole doping drives the Fermi level of the doped Dirac semimetal towards the valence band top, and they coincide in energy at $x \simeq -0.01$, where CO_R sets in via a second-order transition. The coexistence splits mainly the valence bands and pushes one of the valence band top below Fermi level to lower the ground state energy.

IV. SUMMARIES

In this paper, we constructed an effective square lattice single-orbital t-U-V-Γ_2 model for the low-energy physics in Sr$_2$IrO$_4$, where Γ_2 is the in-plane anisotropy of the $J_{\text{eff}} = \frac{1}{2}$ pseudospins arising from the cooperative interplay between Hund's rule coupling and SOC [47]. To study the mean-field ground state properties of the model, the onsite Coulomb repulsion U is treated by SU(2) spin-rotation invariant slave-boson mean-field theory, while nn interactions, V and Γ_2, are mean-field decoupled into bond channels. We obtain the ground state phase diagram at half-filling with fixed $\Gamma_2 = 0.2t_1$, in the plane spanned by U and V, and investigate the competition and coexistence of magnetic and bond orders.

The nn V, which is expected to be significant in Sr$_2$IrO$_4$ due to the large spatial extension of the Ir $5d$ orbitals, is capable of driving dSCO with circulating spin current, which is degenerate in energy with the SFP produced by circulating charge current. We demonstrated the importance of in-plane anisotropy Γ_2 in the stabilization of dSCO. It lifts the degeneracy by stabilizing dSCO and lowers the rotation symmetry of dSCO from SO(3) to C_{4z} with four equivalent preferred directions along [$\pm 1, \pm 1, 0$]. The lifting of degeneracy and the lowering of rotation symmetry are achieved via the development of a s-wave spin current with the spin direction along [$\pm 1, \mp 1, 0$]. It coexists with d-wave χ_{dSCO} and lowers the state energy. The dSCO order gaps out the QBT while leaves the DP unaltered, giving rise to a Dirac semimetal when its amplitude is sufficiently large. Thus, we have succeeded in providing a minimal effective single-orbital model for the hidden electronic order capable of describing the unexpected breaking of spatial symmetries in the AFM ordered spin-orbit Mott insulator in stoichiometric Sr$_2$IrO$_4$ and the unconventional pseudogap phenomena in electron doped Sr$_2$IrO$_4$ [43].

Remarkably, we discovered that, in a wide regime of the phase diagram, the ground state is CO_R, a coexisting phase of AFM, dSCO, and sBN with unconventional right-handed chirality, i.e., ($\hat{e}_{\text{AFM}} \times \hat{e}_{dSCO}$) · $\hat{e}_{\text{sBN}}$ = 1. In this phase, the dSCO order is relatively small, and the Fermi level would cross the valence band near X point in the would-be pure dSCO state. The coexistent state sets in here as the ground state, gaining energy by splitting the bands and pushing one of the valence band below Fermi level. Its chirality leads to uneven splitting of the valence and conduction bands, with CO_R splits mostly the valence band and CO_L splits mainly the conduction bands. We demonstrated that the emergence of coexistent state and its chirality can potentially be manipulated by carrier doping a Dirac semimetal. CO_R with right-handed chirality and CO_L with left-handed chirality can be realized separately by hole and electron doping. The electron doping evolution of the AFM insulator is also investigated. As increases the electron doping concentration x, the ground state undergoes successively first-order phase transitions from the AFM to dSCO, CO_L, and PM.

It would be interesting to investigate if the coexistent phase possesses any nontrival topological properties. In the mean-field study of the t-U-V-Γ_2 model conducted in this work, the coexistent states, either CO_R or CO_L, can emerge only in metallic states, no insulating states with simultaneously developed AFM and dSCO orders have been stabilized. It would be desirable to study the quantum states and phase diagram of this model by more sophisticated analytical and numerical methods for an improved understanding. The findings presented in this work can be viewed as a starting point for further studies.
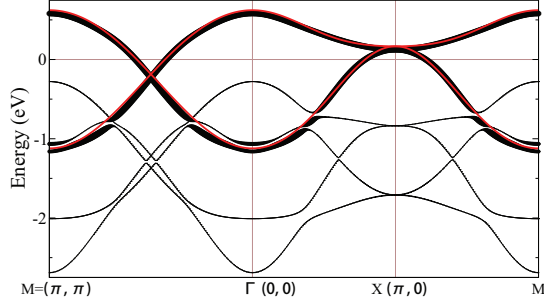
FIG. 9. Band dispersion (red lines) of the single-orbital tight-binding model. The black lines display the interacting electronic structure of undoped Sr_2IrO_4 obtained from the five-orbital model [43] at Hubbard interaction $(U, J_H) = (1.2, 0.05)$ eV, with the line thickness denoting the content of $J_{eff} = 1/2$ doublet.

Appendix A: Single-orbital tight-binding model

In the atomic limit, Ir^{4+} has a $5d^5$ configuration, with 5 electrons occupy the lower threefold t_{2g} orbitals separated from the higher twofold e_g orbitals by the cubic crystal field. The strong atomic SOC splits the t_{2g} orbitals into a low-lying $J_{eff} = \frac{3}{2}$ multiplet occupied by 4 electrons and a singly occupied $J_{eff} = \frac{1}{2}$ doublet. For Sr_2IrO_4 solid, electronic structure calculations using the local-density approximation including SOC and structural distortion shows that, for the realistic bandwidths and crystalline electric field, the atomic SOC is insufficient to prevent two bands of predominantly $J_{eff} = \frac{1}{2}$ and $\frac{3}{2}$ characters to cross the Fermi level and give rise to two Fermi surfaces. It has been shown that electron correlations, i.e., multiorbital Hubbard interaction, leads to a significantly enhanced effective SOC for the t_{2g} complex [3, 43, 62], pushing the $J_{eff} = \frac{3}{2}$ band in the LDA band structure below the Fermi level, and consequently gives rise to the single band crossing the Fermi level that is of dominant $J_{eff} = \frac{1}{2}$ character [1]. This correlation-induced band polarization through enhancement of the SOC by the Hubbard interaction enables the single-orbital model of $J_{eff} = \frac{1}{2}$ electrons for Sr_2IrO_4.

Fig. 9 displays the interacting electronic structure (black lines) of undoped Sr_2IrO_4 obtained from the realistic five-

orbital model [43] at Hubbard interaction $(U, J_H) = (1.2, 0.05)$ eV, with the line thickness denotes the content of the $J_{eff} = \frac{1}{2}$ doublet. The red lines show the single-orbital tight-binding dispersion with hopping parameters chosen according to $t_{ij} = (218, 52, -18)$ meV for the first, second, and third nearest neighbors, respectively. Clearly, the effective single-orbital model describes faithfully the low-energy electronic structure of the interacting Sr_2IrO_4.

	E	C_{4z}	C_{2z}	C_{4z}^{-1}	M_x	M_y	M_{xy}	M_{-xy}
AFM	0	×	τ	×	×	×	τ	0
dSCO	0	×	τ	×	×	×	τ	0
sBN	0	×	$0, \tau$	×	×	×	$0, \tau$	$0, \tau$

	T	TC_{4z}	TC_{2z}	TC_{4z}^{-1}	TM_x	TM_y	TM_{xy}	TM_{-xy}
AFM	τ	×	0	×	×	×	0	τ
dSCO	0	×	τ	×	×	×	τ	0
sBN	×	$0, \tau$	×	$0, \tau$	$0, \tau$	$0, \tau$	×	×

TABLE I. Symmetries of [1, 1, 0]-ordered AFM, [−1, 1, 0]-ordered dSCO, and [0, 0, 1]-ordered sBN states. The table gives the lattice translation required for a state to recover itself after a symmetry operation of the magnetic space group of $4mm1'$. τ is the translation of one lattice constant along either x- or y-axis. Symbol × means such a lattice translation does not exist.

Appendix B: Symmetry analysis

We analyze the symmetry properties of the states considered in this work within the symmetry point group $C_{4v} \otimes \{E, T\}$, i.e., the magnetic point group $4mm1'$, where C_{4v} is the symmetry point group of the two-dimensional square lattice and T is the time-reversal operation. The magnetic point group $4mm1'$ has 16 symmetry operations: the 8 symmetry operations of C_{4v} listed in the top half of Table I and their products with T in the bottom half. The 8 operations are identity E, fourfold rotation around z-axis C_{4z}, twofold rotation around z-axis C_{2z}, inverse fourfold rotation around z-axis C_{4z}^{-1}, mirror reflection about yz-plane M_x, mirror reflection about zx-plane M_y, mirror reflection about diagonal-plane M_{xy}, and mirror reflection about anti-diagonal-plane M_{-xy}. The symmetries of [1, 1, 0]-ordered AFM, [−1, 1, 0]-ordered dSCO, and [0, 0, 1]-ordered sBN are summarized in Table I, which gives the lattice translation, if it exists, required for a state to recover itself after a symmetry operation of the magnetic point group $4mm1'$. The state does not have the corresponding symmetry if it could not recover itself by any lattice translation after a symmetry operation. Clearly, both [1, 1, 0]-ordered AFM and [−1, 1, 0]-ordered dSCO break $\{C_{4z}, C_{4z}^{-1}, M_x, M_y, TC_{4z}, TC_{4z}^{-1}, TM_x, TM_y\}$ symmetries and belong to the magnetic point group $mm21'$, while the [0, 0, 1]-ordered sBN breaks $\{C_{4z}, C_{4z}^{-1}, M_x, M_y, T, TC_{2z}, TM_{xy}, TM_{-xy}\}$ symmetries and belongs to the magnetic point group $4'm'm$.

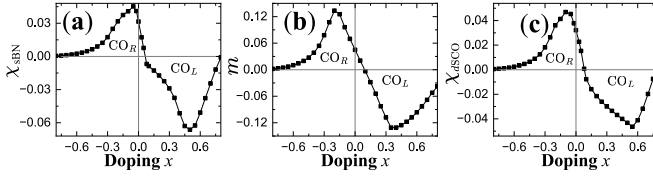Using the symmetries of AFM, dSCO, and sBN listed in Table I, it is straightforward to obtain the symmetries of any

FIG. 10. The expectation of (a) sBN, (b) AFM, and (c) dSCO order as a function of doping concentration x in the phenomenological co-existent state where the other two orders with the strength of 0.05 are introduced manually to the tight-binding model.

coexistent state. The coexistent state has a symmetry only if there exists a lattice translation that simultaneously recovers all involved states after the corresponding symmetry operation. It is thus easy to show that all coexistent states, no matter it consists of any two or all three of AFM, dSCO, and sBN orders, are invariant under $\{E, C_{2z}, M_{xy}, M_{-xy}\}$ operations, and belong to the magnetic group $mm2$. Since they all possess the same symmetry properties, the combination of any two of these three orders would naturally leads to the emergence of the third one. To demonstrate this, we have introduced phenomenologically two of these three orders, of the strength of 0.05, to the tight-binding Hamiltonian, and then calculate the expectation of the third order. The doping dependence of the third order is shown in Fig. 10a for sBN, in Fig. 10b for AFM, and in Fig. 10c for dSCO. Clearly, each of the three orders can be induced by the combination of the other two orders. It varies continuously as a function of doping concentration x, and changes its sign from negative to positive at a critical doping, indicating a transition in its chirality from left-handed to right-handed.

---

* wangzi@bc.edu
† zhousen@itp.ac.cn

[1] B. J. Kim, H. Jin, S. J. Moon, J.-Y. Kim, B.-G. Park, C. S. Leem, J. Yu, T. W. Noh, C. Kim, S.-J. Oh, J.-H. Park, V. Durairaj, G. Cao, and E. Rotenberg, Novel $J_{eff} = 1/2$ Mott State Induced by Relativistic Spin-Orbit Coupling in Sr$_2$IrO$_4$, Phys. Rev. Lett. **101**, 076402 (2008).

[2] B. J. Kim, H. Ohsumi, T. Komesu, S. Sakai, T. Morita, H. Takagi, and T. Arima, Phase-Sensitive Observation of a Spin-Orbital Mott State in Sr$_2$IrO$_4$, Science **323**, 1329 (2009).

[3] D. Pesin and L. Balents, Mott physics and band topology in materials with strong spin-orbit interaction, Nature Physics **6**, 376 (2010).

[4] W. Witczak-Krempa, G. Chen, Y. B. Kim, and L. Balents, Correlated quantum phenomena in the strong spin-orbit regime, Annual Review of Condensed Matter Physics **5**, 57 (2014).

[5] J. G. Rau, E. K.-H. Lee, and H.-Y. Kee, Spin-orbit physics giving rise to novel phases in correlated systems: Iridates and related materials, Annual Review of Condensed Matter Physics **7**, 195 (2016).

[6] R. Schaffer, E. K.-H. Lee, B.-J. Yang, and Y. B. Kim, Recent progress on correlated electron systems with strong spin-orbit coupling, Reports on Progress in Physics **79**, 094504 (2016).

[7] J. Dai, E. Calleja, G. Cao, and K. McElroy, Local density of states study of a spin-orbit-coupling induced Mott insulator Sr$_2$IrO$_4$, Phys. Rev. B **90**, 041102 (2014).

[8] S. M. Winter, A. A. Tsirlin, M. Daghofer, J. van den Brink, Y. Singh, P. Gegenwart, and R. Valentí, Models and materials for generalized kitaev magnetism, Journal of Physics: Condensed Matter **29**, 493002 (2017).

[9] J. Bertinshaw, Y. Kim, G. Khaliullin, and B. Kim, Square lattice iridates, Annual Review of Condensed Matter Physics **10**, 315 (2019).

[10] B. Lenz, C. Martins, and S. Biermann, Spectral functions of Sr$_2$IrO$_4$: theory versus experiment, Journal of Physics: Condensed Matter **31**, 293001 (2019).

[11] C. Lu and J.-M. Liu, The $J_{eff} = 1/2$ Antiferromagnet Sr$_2$IrO$_4$: A golden Avenue toward New Physics and Functions, Advanced Materials **32**, 1904508 (2020).

[12] B. Zwartsenberg, R. P. Day, E. Razzoli, M. Michiardi, N. Xu, M. Shi, J. D. Denlinger, G. Cao, S. Calder, K. Ueda, *et al.*, Spin-orbit-controlled metal–insulator transition in Sr$_2$IrO$_4$, Nature Physics **16**, 290 (2020).

[13] J. Kim, D. Casa, M. H. Upton, T. Gog, Y.-J. Kim, J. F. Mitchell, M. van Veenendaal, M. Daghofer, J. van den Brink, G. Khaliullin, and B. J. Kim, Magnetic Excitation Spectra of Sr$_2$IrO$_4$ Probed by Resonant Inelastic X-Ray Scattering: Establishing Links to Cuprate Superconductors, Phys. Rev. Lett. **108**, 177003 (2012).

[14] S. Calder, D. M. Pajerowski, M. B. Stone, and A. F. May, Spin-gap and two-dimensional magnetic excitations in Sr$_2$IrO$_4$, Phys. Rev. B **98**, 220402 (2018).

[15] F. Wang and T. Senthil, Twisted Hubbard Model for Sr$_2$IrO$_4$: Magnetism and Possible High Temperature Superconductivity, Phys. Rev. Lett. **106**, 136402 (2011).

[16] H. Watanabe, T. Shirakawa, and S. Yunoki, Monte Carlo Study of an Unconventional Superconducting Phase in Iridium Oxide J_{eff}=1/2 Mott Insulators Induced by Carrier Doping, Phys. Rev. Lett. **110**, 027002 (2013).

[17] Y. Yang, W.-S. Wang, J.-G. Liu, H. Chen, J.-H. Dai, and Q.-H. Wang, Superconductivity in doped Sr$_2$IrO$_4$: A functional renormalization group study, Phys. Rev. B **89**, 094518 (2014).

[18] Z. Y. Meng, Y. B. Kim, and H.-Y. Kee, Odd-Parity Triplet Superconducting Phase in Multiorbital Materials with a Strong Spin-Orbit Coupling: Application to Doped Sr$_2$IrO$_4$, Phys. Rev. Lett. **113**, 177003 (2014).

[19] A. de la Torre, S. McKeown Walker, F. Y. Bruno, S. Riccó, Z. Wang, I. Gutierrez Lezama, G. Scheerer, G. Giriat, D. Jaccard, C. Berthod, T. K. Kim, M. Hoesch, E. C. Hunter, R. S. Perry, A. Tamai, and F. Baumberger, Collapse of the Mott Gap and Emergence of a Nodal Liquid in Lightly Doped Sr$_2$IrO$_4$, Phys. Rev. Lett. **115**, 176402 (2015).

[20] Y. K. Kim, O. Krupin, J. D. Denlinger, A. Bostwick, E. Rotenberg, Q. Zhao, J. F. Mitchell, J. W. Allen, and B. J. Kim, Fermi arcs in a doped pseudospin-1/2 Heisenberg antiferromagnet, Science **345**, 187 (2014).

[21] Y. J. Yan, M. Q. Ren, H. C. Xu, B. P. Xie, R. Tao, H. Y. Choi, N. Lee, Y. J. Choi, T. Zhang, and D. L. Feng, Electron-Doped Sr$_2$IrO$_4$: An Analogue of Hole-Doped Cuprate Superconductors Demonstrated by Scanning Tunneling Microscopy, Phys. Rev. X **5**, 041018 (2015).

[22] I. Battisti, K. M. Bastiaans, V. Fedoseev, A. De La Torre, N. Iliopoulos, A. Tamai, E. C. Hunter, R. S. Perry, J. Zaanen, F. Baumberger, *et al.*, Universality of pseudogap and emergent order in lightly doped mott insulators, Nature physics **13**, 21 (2017).

[23] S. Peng, C. Lane, Y. Hu, M. Guo, X. Chen, Z. Sun, M. Hashimoto, D. Lu, Z.-X. Shen, T. Wu, *et al.*, Electronic nature of the pseudogap in electron-doped Sr_2IrO_4, npj Quantum Materials **7**, 58 (2022).

[24] Y. K. Kim, N. Sung, J. Denlinger, and B. Kim, Observation of a *d*-wave gap in electron-doped Sr_2IrO_4, Nature Physics **12**, 37 (2016).

[25] H. Zhao, S. Manna, Z. Porter, X. Chen, A. Uzdejczyk, J. Moodera, Z. Wang, S. D. Wilson, and I. Zeljkovic, Atomic-scale fragmentation and collapse of antiferromagnetic order in a doped mott insulator, Nature Physics **15**, 1267 (2019).

[26] S. Boseggia, H. C. Walker, J. Vale, R. Springell, Z. Feng, R. S. Perry, M. M. Sala, H. M. Rønnow, S. P. Collins, and D. F. McMorrow, Locking of iridium magnetic moments to the correlated rotation of oxygen octahedra in Sr_2IrO_4 revealed by x-ray resonant scattering, Journal of Physics: Condensed Matter **25**, 422202 (2013).

[27] M. K. Crawford, M. A. Subramanian, R. L. Harlow, J. A. Fernandez-Baca, Z. R. Wang, and D. C. Johnston, Structural and magnetic studies of Sr_2IrO_4, Phys. Rev. B **49**, 9198 (1994).

[28] F. Ye, S. Chi, B. C. Chakoumakos, J. A. Fernandez-Baca, T. Qi, and G. Cao, Magnetic and crystal structures of Sr_2IrO_4: A neutron diffraction study, Phys. Rev. B **87**, 140406 (2013).

[29] C. Dhital, T. Hogan, Z. Yamani, C. de la Cruz, X. Chen, S. Khadka, Z. Ren, and S. D. Wilson, Neutron scattering study of correlated phase behavior in Sr_2IrO_4, Phys. Rev. B **87**, 144405 (2013).

[30] D. H. Torchinsky, H. Chu, L. Zhao, N. B. Perkins, Y. Sizyuk, T. Qi, G. Cao, and D. Hsieh, Structural Distortion-Induced Magnetoelastic Locking in Sr_2IrO_4 Revealed through Nonlinear Optical Harmonic Generation, Phys. Rev. Lett. **114**, 096404 (2015).

[31] S. Boseggia, R. Springell, H. C. Walker, H. M. Rønnow, C. Rüegg, H. Okabe, M. Isobe, R. S. Perry, S. P. Collins, and D. F. McMorrow, Robustness of Basal-Plane Antiferromagnetic Order and the J_{eff}=1/2 State in Single-Layer Iridate Spin-Orbit Mott Insulators, Phys. Rev. Lett. **110**, 117207 (2013).

[32] L. Zhao, D. Torchinsky, H. Chu, V. Ivanov, R. Lifshitz, R. Flint, T. Qi, G. Cao, and D. Hsieh, Evidence of an odd-parity hidden order in a spin–orbit coupled correlated iridate, Nature Physics **12**, 32 (2016).

[33] S. Di Matteo and M. R. Norman, Magnetic ground state of Sr_2IrO_4 and implications for second-harmonic generation, Phys. Rev. B **94**, 075148 (2016).

[34] K. L. Seyler, A. de la Torre, Z. Porter, E. Zoghlin, R. Polski, M. Nguyen, S. Nadj-Perge, S. D. Wilson, and D. Hsieh, Spin-orbit-enhanced magnetic surface second-harmonic generation in Sr_2IrO_4, Phys. Rev. B **102**, 201113 (2020).

[35] J. Jeong, Y. Sidis, A. Louat, V. Brouet, and P. Bourges, Time-reversal symmetry breaking hidden order in $Sr_2(Ir, Rh)O_4$, Nature communications **8**, 15119 (2017).

[36] C. Tan, Z. F. Ding, J. Zhang, Z. H. Zhu, O. O. Bernal, P. C. Ho, A. D. Hillier, A. Koda, H. Luetkens, G. D. Morris, D. E. MacLaughlin, and L. Shu, Slow magnetic fluctuations and critical slowing down in $Sr_2Ir_{1-x}Rh_xO_4$, Phys. Rev. B **101**, 195108 (2020).

[37] X. Chen, J. L. Schmehr, Z. Islam, Z. Porter, E. Zoghlin, K. Finkelstein, J. P. Ruff, and S. D. Wilson, Unidirectional spin density wave state in metallic $(Sr_{1-x}La_x)_2IrO_4$, Nature communications **9**, 103 (2018).

[38] H. Murayama, K. Ishida, R. Kurihara, T. Ono, Y. Sato, Y. Kasahara, H. Watanabe, Y. Yanase, G. Cao, Y. Mizukami, T. Shibauchi, Y. Matsuda, and S. Kasahara, Bond Directional Anapole Order in a Spin-Orbit Coupled Mott Insulator $Sr_2(Ir_{1-x}Rh_x)O_4$, Phys. Rev. X **11**, 011021 (2021).

[39] C. M. Varma, Non-fermi-liquid states and pairing instability of a general model of copper oxide metals, Phys. Rev. B **55**, 14554 (1997).

[40] C. M. Varma, Theory of the pseudogap state of the cuprates, Phys. Rev. B **73**, 155113 (2006).

[41] C. M. Varma, Pseudogap in cuprates in the loop-current ordered state, Journal of Physics: Condensed Matter **26**, 505701 (2014).

[42] S. J. Moon, M. W. Kim, K. W. Kim, Y. S. Lee, J.-Y. Kim, J.-H. Park, B. J. Kim, S.-J. Oh, S. Nakatsuji, Y. Maeno, I. Nagai, S. I. Ikeda, G. Cao, and T. W. Noh, Electronic structures of layered perovskite Sr_2MO_4 (*M* = Ru, Rh, and Ir), Phys. Rev. B **74**, 113104 (2006).

[43] S. Zhou, K. Jiang, H. Chen, and Z. Wang, Correlation Effects and Hidden Spin-Orbit Entangled Electronic Order in Parent and Electron-Doped Iridates Sr_2IrO_4, Phys. Rev. X **7**, 041018 (2017).

[44] Y.-P. Huang, J.-W. Dong, Z. Wang, and S. Zhou, Three-dimensional stacking of canted antiferromagnetism and pseudospin current in undoped Sr_2IrO_4: Symmetry analysis and microscopic model realization, Phys. Rev. B **104**, 165145 (2021).

[45] J. W. Han, S.-W. Kim, W. S. Kyung, C. Kim, G. Cao, X. Chen, S. D. Wilson, S. Cheon, and J. S. Lee, Nonsymmorphic Dirac semimetal and carrier dynamics in the doped spin-orbit-coupled Mott insulator Sr_2IrO_4, Phys. Rev. B **102**, 041108 (2020).

[46] S.-W. Kim, M. Kang, and S. Cheon, Low-energy electrodynamics of Dirac semimetal phases in the doped Mott insulator Sr_2IrO_4, Phys. Rev. B **103**, 045116 (2021).

[47] G. Jackeli and G. Khaliullin, Mott insulators in the strong spin-orbit coupling limit: From heisenberg to a quantum compass and kitaev models, Phys. Rev. Lett. **102**, 017205 (2009).

[48] S. Raghu, X.-L. Qi, C. Honerkamp, and S.-C. Zhang, Topological mott insulators, Phys. Rev. Lett. **100**, 156401 (2008).

[49] T. Li, P. Wölfle, and P. J. Hirschfeld, Spin-rotation-invariant slave-boson approach to the hubbard model, Phys. Rev. B **40**, 6817 (1989).

[50] R. Frésard and P. Wölfle, Unified slave boson representation of spin and charge degrees of freedom for strongly correlated fermi systems, International Journal of Modern Physics B **6**, 685 (1992).

[51] K. Jiang, S. Zhou, and Z. Wang, Textured electronic states of the triangular-lattice Hubbard model and Na_xCoO_2, Phys. Rev. B **90**, 165135 (2014).

[52] Y.-P. Huang, J.-W. Dong, P. Kotetes, and S. Zhou, Antiferromagnetic chiral spin density wave and strain-induced Chern insulator in the square lattice Hubbard model with frustration, Phys. Rev. B **102**, 195120 (2020).

[53] K. Jiang, J. Hu, H. Ding, and Z. Wang, Interatomic coulomb interaction and electron nematic bond order in FeSe, Phys. Rev. B **93**, 115138 (2016).

[54] Y. Hong, Y. Jo, H. Y. Choi, N. Lee, Y. J. Choi, and W. Kang, Large magnetic anisotropy in canted antiferromagnetic Sr_2IrO_4 single crystals, Phys. Rev. B **93**, 094406 (2016).

[55] M. Nauman, Y. Hong, T. Hussain, M. S. Seo, S. Y. Park, N. Lee, Y. J. Choi, W. Kang, and Y. Jo, In-plane magnetic anisotropy in strontium iridate Sr_2IrO_4, Phys. Rev. B **96**, 155102 (2017).

[56] M. Nauman, T. Hussain, J. Choi, N. Lee, Y. J. Choi, W. Kang, and Y. Jo, Low-field magnetic anisotropy of Sr_2IrO_4, Journal of Physics: Condensed Matter **34**, 135802 (2022).

[57] H. Zhou, Y.-Y. Xu, and S. Zhou, Electron Correlations, Spin-Orbit Coupling, and Antiferromagnetic Anisotropy in Layered Perovskite Iridates Sr_2IrO_4, Communications in Theoretical Physics **70**, 081 (2018).

[58] S. Mohapatra and A. Singh, Pseudo-spin rotation symmetry

breaking by coulomb interaction terms in spin–orbit coupled systems, Journal of Physics: Condensed Matter **33**, 065802 (2020).

[59] H. Liu and G. Khaliullin, Pseudo-jahn-teller effect and magnetoelastic coupling in spin-orbit mott insulators, Phys. Rev. Lett. **122**, 057203 (2019).

[60] S. Zhou and Z. Wang, Electron Correlation and Spin Density Wave Order in Iron Pnictides, Phys. Rev. Lett. **105**, 096401 (2010).

[61] X. Chen, T. Hogan, D. Walkup, W. Zhou, M. Pokharel, M. Yao, W. Tian, T. Z. Ward, Y. Zhao, D. Parshall, C. Opeil, J. W. Lynn, V. Madhavan, and S. D. Wilson, Influence of electron doping on the ground state of $(Sr_{1-x}La_x)_2IrO_4$, Phys. Rev. B **92**, 075125 (2015).

[62] K. Jiang, Correlation renormalized and induced spin-orbit coupling, Chinese Physics Letters **40**, 017102 (2023).